Disorder and localization effects on the local spectroscopic and infrared optical properties of Ga$_{1-x}$Mn$_x$As

Huawei Gao,[1,2,*] Cristian Cernov,[2] T. Jungwirth,[3,4] and Jairo Sinova[1,2,3]

[1]*Institut für Physik, Johannes Gutenberg Universität Mainz, 55128 Mainz, Germany*
[2]*Department of Physics, Texas A&M University, College Station, Texas 77843-4242, USA*
[3]*Institute of Physics ASCR, v.v.i., Cukrovarnická 10, 162 53 Praha 6, Czech Republic*
[4]*School of Physics and Astronomy, University of Nottingham, Nottingham NG7 2RD, United Kingdom*

We study numerically the influence of disorder and localization effects on the local spectroscopic characteristics and infrared optical properties of Ga$_{1-x}$Mn$_x$As. We treat the band structure and disorder effects at an equal level by using an exact diagonalization supercell simulation method. This method accurately describes the low-doping limit and gives a clear picture of the transition to higher dopings, which captures the localization effects inaccessible to other theoretical methods commonly used. Our simulations capture the rich in-gap localized states observed in scanning tunneling microscopy studies and reproduce the observed features of the infrared optical absorption experiments. We show clear evidence of a disordered-valence-band model for metallic samples in which (i) there is no impurity band detached from the valence band, (ii) the disorder tends to localize and pull states near the top of the valence band into the gap region, and (iii) the Fermi energy is located deep in the delocalized region away from the mobility edge. We identify localized states deep in the gap region by visualizing the probability distribution of the quasiparticles and connecting it to their respective participation ratios. The analysis of the infrared optical absorption data indicates that it does not have a direct relation to the nature of the states at the Fermi energy.

I. INTRODUCTION

Ga$_{1-x}$Mn$_x$As is a material system prototype which incorporates carrier-mediated ferromagnetism into semiconductors [1–5]. Under equilibrium growth conditions, the solubility of Mn in GaAs is limited to ~0.1%. Through the nonequilibrium low-temperature molecular-beam-epitaxy (LT-MBE) technique, highly Mn-doped samples with more than 1% Mn can be obtained [6,7]. As has been shown in a recent systematic study [8,9], high-quality homogeneous samples with reproducible characteristics can be prepared by introducing optimization of growth and postgrowth annealing procedures for each doping concentration. Although its potential for applications has been curtailed due to growth limitations for achieving magnetic transition at room temperature, Ga$_{1-x}$Mn$_x$As is a promising material for testing known magnetotransport, magneto-optical mechanisms, and discovery of new magnetic phenomena [3,4].

However, even after many recent studies on this material, a common debate still exists regarding the electronic states near the top of the valence band and at the Fermi energy [10]. At small Mn doping, $x \lesssim 0.1\%$, Ga$_{1-x}$Mn$_x$As is insulating and paramagnetic. The bound-hole states introduced by Mn form an impurity band (IB) *detached* from the top of the GaAs valence band (VB). For higher Mn doping, $0.5\% \lesssim x \lesssim 1.5\%$, the overlap between bound-hole states is sufficiently large that the IB starts mixing with the VB. The material is still insulating but ferromagnetism begins to occur. At $x \sim 1.5\%$, the abrupt increase of low-temperature conductivity shows that the material becomes a degenerate semiconductor. In this metallic regime, one proposal states that the IB merges with the VB, forming a disordered VB [10]. Another proposal assumes that the Fermi level still resides in the narrow IB, detached from the VB [7]. However, the latter proposal, based on early spectroscopic studies on unoptimized samples [6,7],

is inconsistent with recent spectroscopic studies [9]. It has also been shown to be inconsistent with microscopic band structure theories[11]. In this paper, through a more realistic treatment of disorder effects extrapolated from the low- to the high-doping regimes, we show clear evidence of a disordered-valence-band model for metallic samples in which (i) there is no impurity band detached from the valence band, (ii) the disorder tends to localize and pull states near the top of the valence band into the gap region, and (iii) the Fermi energy is located deep in the delocalized region away from the mobility edge.

Some early numerical studies either ignored disorder effects or treated them in the framework of mean-field theory [12–16]. In order to treat these effects more realistically, we use the exact diagonalization supercell method [17]. The advantage of this method is that the band structure and disorder effects are captured at an equal level which allows the study of disorder and localization effects on the local spectroscopic characteristics and infrared optical properties of Ga$_{1-x}$Mn$_x$As. The Hamiltonian includes the $\vec{k} \cdot \vec{p}$ description of the GaAs valence band, the Coulomb interactions at the Hartree level, a short-range central-cell potential, and the kinetic exchange interaction. By diagonalizing this Hamiltonian numerically in the framework of the envelope function approximation [18], eigenvalues and eigenfunctions can be obtained. Our wave function probability distribution visualization shows clear hydrogeniclike bound states for nearly isolated Mn impurities in low-doped samples as well as the transition of these bound states to higher-doped samples. The (local) density of states (LDOS or DOS) calculations capture the rich in-gap localized states observed in scanning tunneling microscopy studies [19]. The optical conductivity calculations reproduce the observed broad peak at ~200 meV of the infrared optical absorption measurements [6,8]. An analysis of the optical absorption data show no direct relation of these data to the nature of the states at the Fermi energy, contradicting the implied connection assumed by the IB models.

————
*gaohuawei@tamu.edu

The paper is organized as follows. Section II comprises a brief introduction of our simulation Hamiltonian. Section III provides the simulation results and discussion. In this section, we study the bound-state properties in the low-Mn-doping limit first, then the DOS and LDOS in the high-concentration regime, followed by an analysis of the localized properties of the states, and finally the ac-conductivity calculations. Section IV presents the conclusions.

II. MODEL HAMILTONIAN

We use a phenomenological model employed by Yang *et al.* [17]. In this model, the valence band of the host semiconductor GaAs is described by the six-band $\vec{k} \cdot \vec{p}$ Kohn-Luttinger model [20]. Within the single-particle approximation, the hole carriers interact with randomly placed Mn local moments via the Coulomb and the exchange interactions [21]. A short-range central-cell correction is also considered in order to capture the difference in the electronegativity of the Mn and host Ga atoms [22]. The choice of this effective model of $Ga_{1-x}Mn_xAs$ that we use in our calculations is justified by the following observations: Density functional theory calculations of the band structure of $Ga_{1-x}Mn_xAs$ are in agreement with the photoemission measurements [23,24]. Microscopic multiorbital tight-binding Anderson calculations of the $Ga_{1-x}Mn_xAs$ band structure, which are in broad agreement with the density functional theory [11], provide a direct link between microscopic electronic structure calculations and the effective kinetic-exchange model we use in our simulations [11]. In $Ga_{1-x}Mn_xAs$, the states near the Fermi energy are formed by *sp* orbitals with moderately hybridized Mn *d* states [11,23,24]. The effective *sp-d* kinetic-exchange model is derived from the microscopic tight-binding Anderson Hamiltonian by performing the Schrieffer-Wolf transformation of the *sp-d* hybridization (and Coulomb interaction) into an effective exchange coupling between magnetic moments and carrier spins [3]. The two descriptions are therefore related by a rigorous transformation and the resulting band structures in both cases are comparably affected by the presence of Mn moments, and both differ significantly from the host GaAs valence bands. In the kinetic-exchange model the transformed *sp* orbitals represent effective wave functions, not the microscopic atomic wave functions. The transformation of the microscopic *sp-d* hybridization, combined with a mean-field description of the magnetic state, yields the exchange splitting of these effective *sp* bands. In real samples, there are charge and magnetic moment compensations due to As antisites and Mn interstitials. In this paper, we consider only the charge compensation introduced by As antisites because the magnetic moment compensation can be reduced by annealing procedures. The total Hamiltonian is given by

$$\hat{H} = \hat{H}^L + \sum_{I=1}^{N_{Mn}} \vec{S}_I \cdot \vec{s}\, J(\vec{r} - \vec{R}_I)$$
$$+ \sum_{I=1}^{N_{Mn}} \left(-\frac{e^2}{\epsilon |\vec{r} - \vec{R}_{Mn,I}|} - V_0 e^{-|\vec{r} - \vec{R}_{Mn,I}|^2 / r_0^2} \right) \hat{I}$$
$$+ \sum_{K=1}^{N_{As}} \frac{2e^2}{\epsilon |\vec{r} - \vec{R}_{As,K}|} \hat{I}, \quad (1)$$

where $\hat{H}^L$ describes the host valence band, the V_0 term is the central-cell correction, $J(\vec{r}) = J_{pd}/[(2\pi a_0^2)^{3/2}]e^{-r^2/2a_0^2}$, $\hat{I}$ is a 6×6 unit matrix, and $\vec{s} = (\hat{s}_x, \hat{s}_y, \hat{s}_z)$, where $\hat{s}_{x,y,z}$ are 6×6 matrices which describe hole spins [25]. $\vec{R}_{Mn,I}$ and $\vec{R}_{As,K}$ are the positions of Mn and As, respectively. The number of holes is given by the relation $N_h = N_{Mn} - 2N_{As}$.

Our numerical method diagonalizes the single-particle Hamiltonian exactly within a finite-size cubic supercell with periodic boundary conditions. In the supercell, Mn and As antisites are randomly distributed within the lattice and Mn spins are described by the classical 5/2 local moments which are aligned in the z direction at zero temperature. The phenomenological parameters we use are the same as the parameters in Ref. [17]. We also treat the mutual interaction between holes by finding the self-consistent solution of the Hartree potential. We use a $6 \times 6 \times 6$ nm^3 cube throughout our simulation.

III. RESULTS AND DISCUSSION

A. Low-doping limit: Bound holes and pair-bonding states

The advantage of our method is the ability to capture the low- as well as the high-Mn-doping limit. In this section, we first study the low limit where there is only a single Mn impurity in our simulation supercell (0.02% Mn). Figure 1 clearly shows a hydrogeniclike bound state with a Bohr radius of $\sim 2a_{lc}$–$3a_{lc}$, where $a_{lc} = 0.565$ nm is the lattice constant of GaAs. This size matches with the experimentally reported value of 20 Å [19]. The outer box shows our simulation supercell, and the lattice structure inside follows the actual lattice constant with respect to the box. The position of the Mn, shown as the light sphere in the middle of the distribution, is randomly chosen. The binding energy of this bound state is
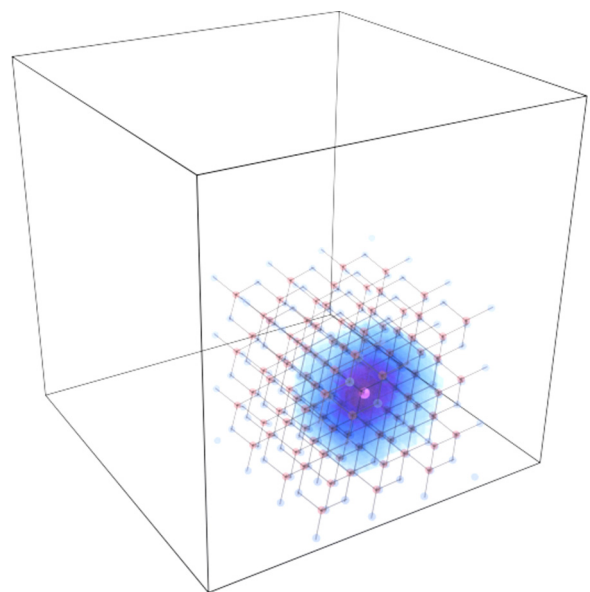

FIG. 1. (Color online) Wave function probability distribution of a single hole with a single Mn impurity in our supercell (black cubic outline). The lattice structure shown depicts the actual lattice constant with respect to the size of the supercell. The light-color sphere in the center of the cloud is the Mn impurity.
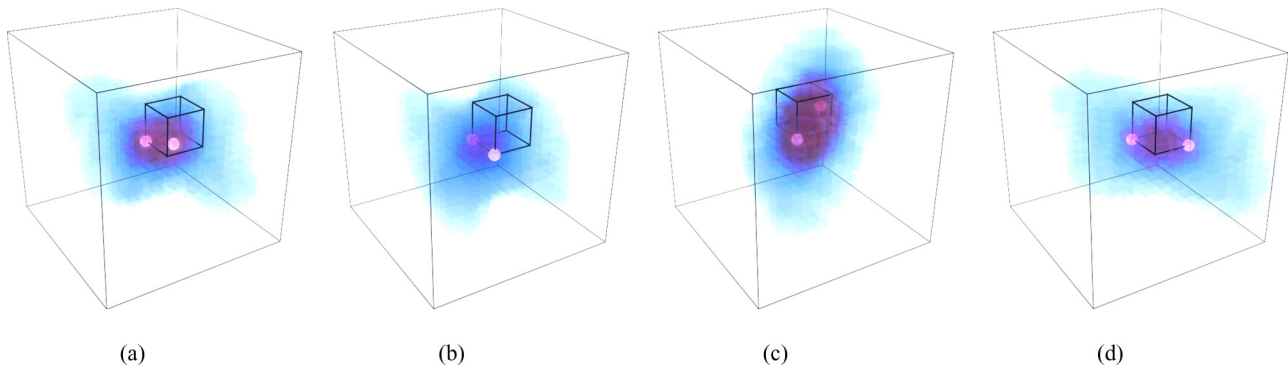
FIG. 2. (Color online) Wave function probability distribution for quasiparticle state with two Mn impurities as the first- to the fourth-nearest neighbors with respect to each other. The outer boxes are not the exact size of our simulation supercells. Light-color spheres are the Mn and the small inner cubes show the actual size of the unit cell of GaAs. (a) First-nearest-neighbor Mn with binding energy 276 meV; (b) second-nearest-neighbor Mn with binding energy 232 meV; (c) third-nearest-neighbor Mn with binding energy 222 meV; (d) fourth-nearest-neighbor Mn with binding energy 199 meV.

$\sim$40 meV, which is about 1/3 of the experimental value for isolated Mn. The results approach the experimental value with an increase in size of our simulation cell and the number of k points for the envelope function expansion.

If two bound states are placed close to one another, one expects that bonding and antibonding states will be formed due to the interaction between the states. Depending on the strength of interaction due to this overlap, the energy difference can be very large. In our case, the bonding state will move deeper in the gap while the antibonding state will move to the valence-band region. Figure 2 shows our simulation results for the bonding state of two Mn impurities. Arranged from first- to fourth-nearest-neighbor positions, the binding energies are 276, 232, 222, and 199 meV, respectively. To provide a better visualization, the images show a zoomed-in view of the probability distribution function, i.e., the outer box outline is not the actual size of our simulation; however, the inner cubic outline is the actual size of the lattice structure with respect to the probability distribution. The highly anisotropic structure of the probability distribution is consistent with STM experiments [26]. As expected, the bonding states have much larger binding energies than the isolated bound states.

B. High-doping regime

1. DOS and LDOS

The impurity-band model assumes that a detached band still persists in the high-doping limit. In this section, we evaluate this high-doping regime by studying the density of states and local density of states in order to confirm whether or not the detached impurity band persists. Our model can give only a qualitative result which is enough to capture the characteristics of the DOS and LDOS. As we know from the previous discussion, two nearby bound states will form bonding and antibonding states. In the high-doping limit, there are many impurity pairs which give rise to a great amount of bonding states in the gap region. On the other hand, the antibonding states will contribute a large number of states to the valence-band region.

The total DOS can capture the distribution of these states. Figure 3 shows the DOS plots for 5% Mn doping, without

As antisite compensation. This figure shows the DOS with and without exchange interactions, i.e., ferromagnetic and nonferromagnetic phases, as well as the DOS obtained from the virtual crystal approximation (VCA) [27]. The VCA assumes that the wave vectors k remain good quantum numbers with disorder treated as an energy spectrum broadening. As shown in the DOS plot, the VCA can change the structure of the valence band only by slightly shifting the energy levels into the gap, whereas our more realistic treatment of disorder tends to pull states near the top of the valence band deeper into the gap region. The kinetic-exchange interaction further splits energy levels and redistributes the states in the gap. As expected, there is an extensive weight of the DOS in the in-gap region which arises from the deep bonding states created by neighboring impurities. However, these DOS curves show only a disordered
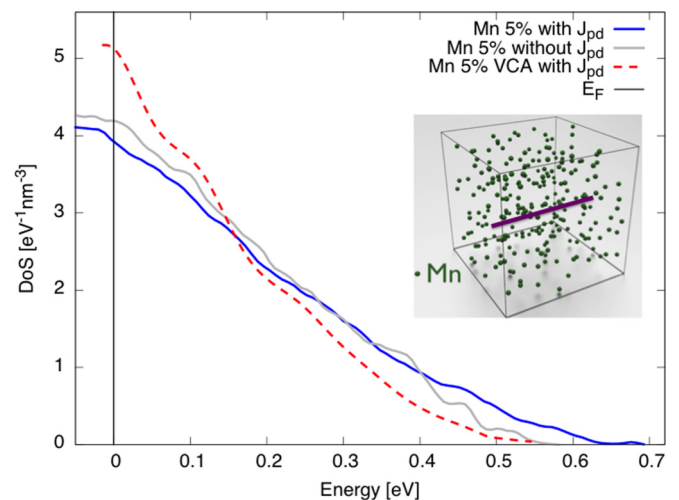

FIG. 3. (Color online) Density of states with and without exchange interactions for 5% Mn doping without As compensation. We shift all the curves to make the Fermi energies zero as the vertical line shows. The red dashed curve is the DOS obtained from the VCA with an energy level broadening of 60 meV. The inset shows one typical Mn distribution in our simulation cell. The purple line in the cell shows the coordinate of the LDOS calculation (shown in Fig. 4).
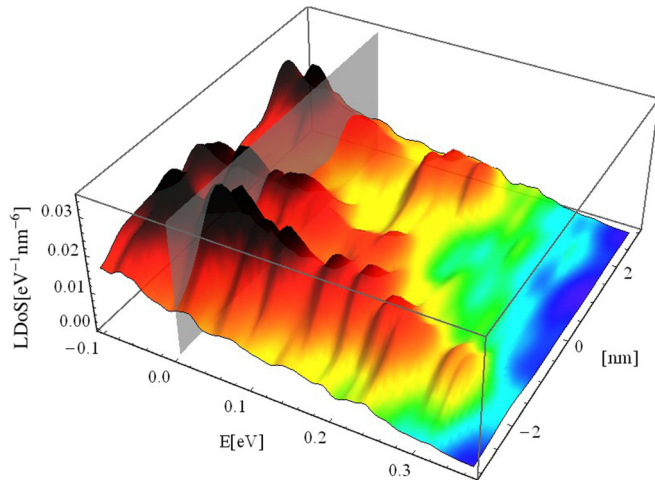
FIG. 4. (Color online) Local density of states for 5% Mn density without As compensation. This plot shows different positions along the x-axis of our simulation supercell which is shown in Fig. 3. The vertical plane shows the position of the Fermi energy. This plot shows no evidence of a detached IB and agrees qualitatively with the STM experiments in Ref. [19].

valence band as opposed to an impurity band detached from the top of the valence band.

To further study the spatial inhomogeneity of the distribution of states in the gap region, we calculate the LDOS, which can be qualitatively compared with the results of STM experiments. Figure 4 shows our simulation results along a line in our simulation cell. The gray vertical plane is the Fermi energy. The peaks formed by bonding states in the gap region are qualitatively consistent with the STM observed features [19], which indicates that our model captures the disorder effects correctly. We emphasize that the comparison between our result and the STM study can only be qualitative. Our model is designed to capture optimized samples, where it shows often semiquantitative agreement with experiments. The STM study [19] was performed on samples which were not fully optimized for each nominal doping (see Ref. [9] for details of the optimized synthesis of $Ga_{1-x}Mn_xAs$); hence our comparison is limited to a qualitative level. Also, we have ignored the Fock-exchange term in the electron-electron interaction in our simulation, which means that we cannot capture the expected reduction of the DOS at the Fermi energy in disordered systems.

2. Localization properties of the states in the high-doping regime

From our DOS study, an impurity band detached from the valence band does not persist for high Mn doping. To further confirm this observation, we study the localization character of the states throughout the spectrum. If an impurity band were to exist in the high-doping limit, we would expect localized states in both tails of the impurity band. As we have shown, bound states in the low-Mn-doping limit ($<0.1\%$) are well localized, indicating the existence of an impurity band for this limit. The probability distribution of these wave functions are concentrated in a small region with a size of several GaAs lattice constants. When the Mn doping is increased, some of

the hole states which are well isolated from others will stay localized, but for some others their wave functions begin to overlap with each other, leading to delocalization. To have a quantitative description of localized and delocalized states, we use participation ratios (PRs) to characterize the extent of localization of states and compare with the probability distributions directly to establish the criteria for localized states. Then we group these states as localized and delocalized based on this criterion. The results show that our model is able to capture the localization physics with its more realistic treatment of disorder. The PR is defined as the inverse of the integral over the simulation volume of the wave function to the fourth power [28,29]

$$PR = \frac{1}{V \int_V d^3r |\Psi(\vec{r})|^4}, \qquad (2)$$

where V is the volume of the simulation cell and $\Psi(\vec{r})$ is the normalized wave function. A simple example gives the meaning of the PR. For delocalized states, $|\Psi(\vec{r})|^2 \sim 1/V$, so PR ~ 1, but for localized states, the wave function probability is concentrated in an area much smaller than V. The PR has the order of $1/V$, which is much smaller than 1 if V is large enough. Another way of distinguishing localized and delocalized states is using size scaling of the PRs. With this method, PRs are calculated as a function of the finite cell size V. This function is almost constant for delocalized states, but scales as $1/V$ for localized states. The disadvantage of using the size scaling of the PR is the computation time because several different cell sizes should be calculated. In this paper, as in other studies in disordered systems, we use the magnitude of the PR and relate it to the probability distribution for hole-state wave functions to distinguish localized and delocalized states.

Figure 5 shows the participation ratios as a function of energy and the typical wave function probability distributions with different participation ratios. For our choice of V, states with PR < 0.1 are localized states with their wave functions concentrated in a small area. For PR > 0.1 but close to 0.1, these states are a transition from localized to delocalized states which define the mobility edge. Within this definition there is of course no sharp separation of localized and delocalized states. This would require the use of the finite-size-scaling method. However, for the purposes of our study it suffices to treat states with PR < 0.1 as localized and above it as delocalized. With this criterion, the red region in Fig. 6 shows the area of the localized states in the DOS plot, meaning that states deep in the gap are well localized, which is consistent with our previous discussion. These states are bonding states formed by nearby Mn impurity pairs with strong interactions. However, if more Mn atoms are doped into this system, localized holes have more places to hop around, becoming delocalized, due to the increasing number of nearby Mn atoms. There will be fewer localized states for samples with higher Mn doping. Figure 7 shows the simulated results for different Mn doping without compensation obtained by averaging over four disorder realizations. It is clear that the number of localized states decreases with increasing Mn doping. In our results only states deep in the gap region are localized far away from the Fermi energy, which does not support the impurity-band picture.
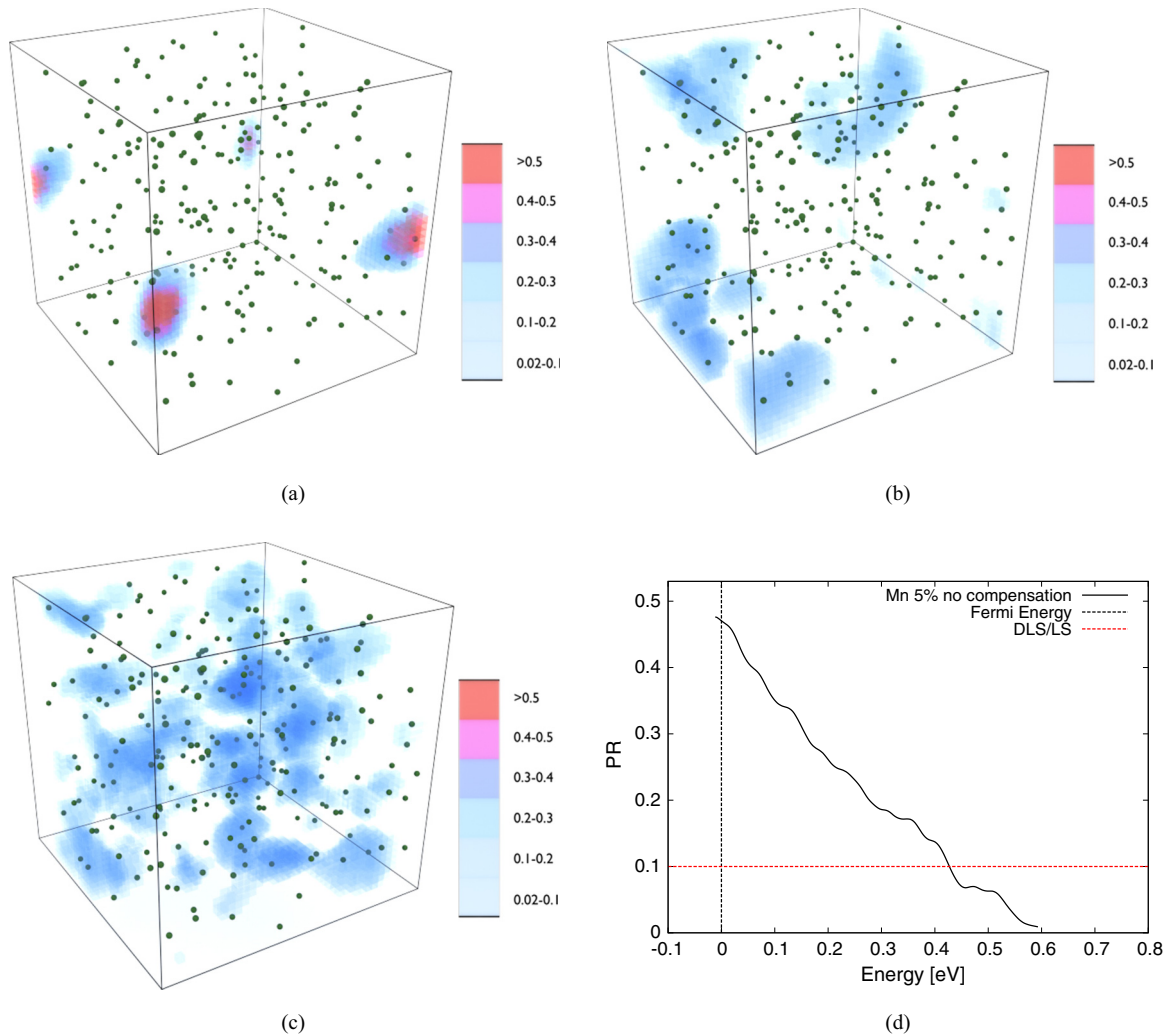
(a)

(b)

(c)

(d)

FIG. 5. (Color online) Wave function probability distribution with a PR of (a) 0.015, (b) 0.1, and (c) 0.2 (green spheres denote Mn impurities). (d) Participation ratios.

C. ac conductivity

In this part, we will study the ac conductivity to explain the spectroscopic experimental observation which was used to
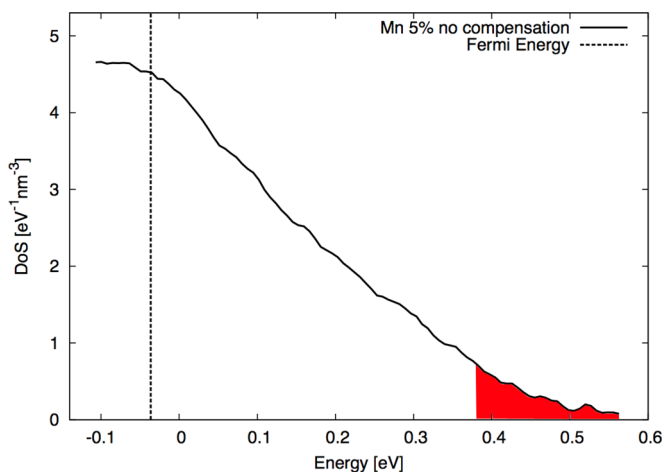

FIG. 6. (Color online) Density of states for 5% Mn without As compensations. Red area shows the localized states

support the impurity-band model. The method used here is the standard linear response Kubo formalism. Early experiments on infrared ac conductivity measurements on $Ga_{1-x}Mn_xAs$ show a broad peak near 200 meV for metallic samples. A redshift was observed when hole concentration was increased, which is the key evidence for the impurity-band model [7]. Later on, similar experiments on optimized growth and postgrowth-annealed samples show a blueshift when the hole concentration was increased [8]. By postgrowth-annealing procedures, the density of compensating defects and other unintentional impurities can be greatly reduced. To compare with these experiments, we will study uncompensated samples first. Figure 8 shows the ac conductivity for Mn dopings ranging from 1% to 5% without compensation. For each doping rate, we do see a broad peak in the low-energy region at ∼100 meV. With increasing Mn doping, there is a redshift when the Mn content is less than 3% and no shift for higher dopings. We expect that compensation plays an important role. Aside from the peak at ∼100 meV, there is one other peak at ∼800 meV for samples with lower Mn doping, which arises from an unphysical finite-size effect and band cutoff for the purposes of the calculation. To study the effects of
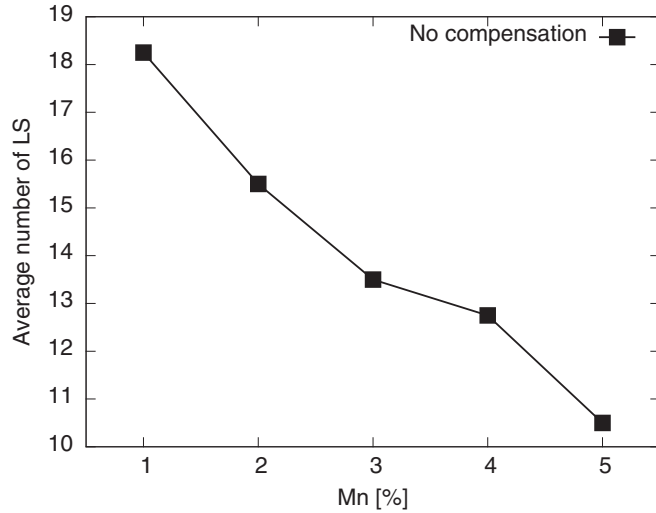
FIG. 7. Average number of localized states in our simulation cell as a function of Mn doping rate.

FIG. 9. (Color online) Real part of σ_{xx} for 5% Mn doping and different hole densities due to As compensation. Data are obtained by averaging over four disorder realizations.

compensation, we fix the Mn doping to be 5% and consider As antisites as a source of hole compensation. Figure 9 shows our simulated results for different hole densities. Compared to the uncompensated samples, the peaks are now shifted from ~100 to ~200 meV. There is still no prevailing redshift with increasing hole density.

The simulated results show that our model is able to capture the mid-infrared peak in optical absorption measurements by considering the transitions from states below the Fermi energy to states above the Fermi energy and deep in the gap region. The Fermi energy resides in the delocalized disordered GaAs valence-band region. This demonstrates that the assumption of the detached IB model is not valid from its starting point in such metallic samples. As shown in the ac-conductivity simulation, the peaks for compensated samples move towards higher energy compared to uncompensated samples. Hence one can get any pattern of the peak shifts if less and more compensated (annealed and unannealed) samples are mixed.
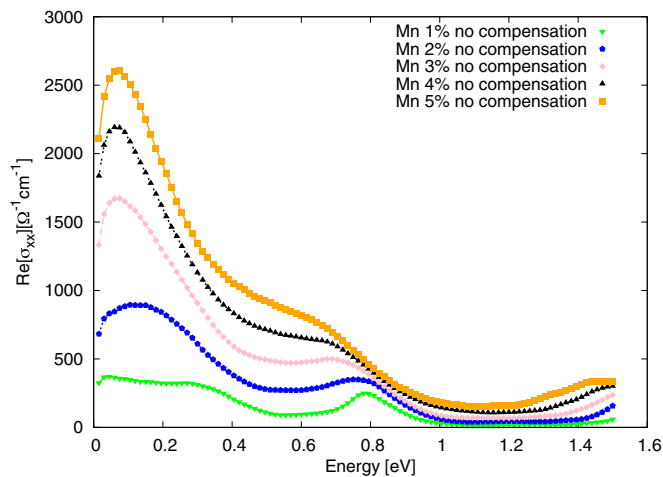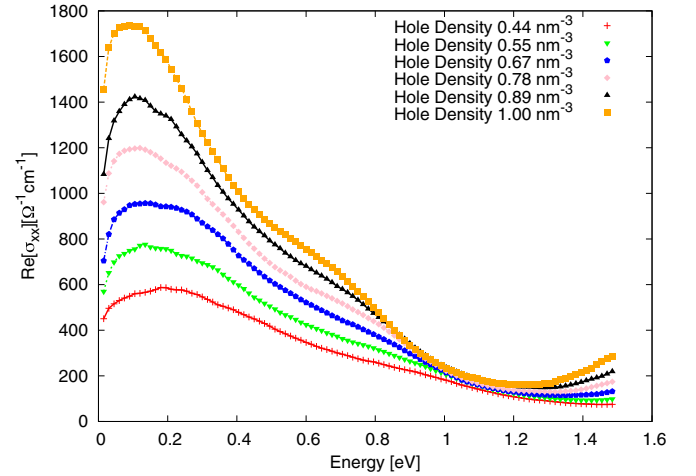

FIG. 8. (Color online) Real part of σ_{xx} for various Mn densities without As compensation. Data obtained by averaging over four disorder realizations.

Experimentally, the actual density of compensation defects is hard to determine. Aside from As antisites, there are other types of charge and moment compensation. So, based on our simulations, the experimentally observed shifts of the ~200 meV peak cannot be used to make any direct conclusions regarding the nature of states at the Fermi energy.

IV. CONCLUSIONS

In this paper, we provide a numerical study of the effects of disorder and localization on the states near the top of the valence band and in the gap region of Mn-doped GaAs. Through exact diagonalization of our model Hamiltonian, the low- and high-doping limits are captured. The local spectroscopic properties are studied and compared with STM experimental results by simulating the DOS and LDOS. Furthermore, via visualization of the probability distribution of the quasiparticles and the connection to their respective participation ratios, we separate the states into localized and delocalized. It is shown for metallic samples that the states deep in the energy gap are well localized and states near the Fermi energy are delocalized. The optical conductivity with different amounts of Mn doping and As compensation is then simulated. Our results show that the peak at ~200 meV is due to the transition of states below the Fermi energy to states in the gap region. There is no direct relation between the optical absorption measurements and the nature of states at the Fermi energy. Our overall results are consistent with the disordered-valence-band model and disagree with the assumption of the IB models of an impurity band detached from the valence band.

[1] H. Ohno, Science **281**, 951 (1998).

[2] H. Ohno, H. Munekata, T. Penney, S. von Molnár, and L. L. Chang, Phys. Rev. Lett. **68**, 2664 (1992).

[3] T. Jungwirth, J. Sinova, J. Mesek, J. Kucera, and A. H. MacDonald, Rev. Mod. Phys. **78**, 809 (2006).

[4] T. Jungwirth, J. Wunderlich, V. Novak, K. Olejnik, B. L. Gallagher, R. P. Campion, K. W. Edmonds, A. W. Rushforth, A. J. Ferguson, and P. Nemec, Rev. Mod. Phys. **86**, 855 (2014).

[5] T. Dietl and H. Ohno, Rev. Mod. Phys. **86**, 187 (2014).

[6] E. J. Singley, R. Kawakami, D. D. Awschalom, and D. N. Basov, Phys. Rev. Lett. **89**, 097203 (2002).

[7] K. S. Burch, D. B. Shrekenhamer, E. J. Singley, J. Stephens, B. L. Sheu, R. K. Kawakami, P. Schiffer, N. Samarth, D. D. Awschalom, and D. N. Basov, Phys. Rev. Lett. **97**, 087208 (2006).

[8] T. Jungwirth, P. Horodyska, N. Tesarova, P. Nemec, J. Subrt, P. Maly, P. Kuzel, C. Kadlec, J. Masek, I. Nemec, M. Orlita, V. Novak, K. Olejnik, Z. Soban, P. Vasek, P. Svoboda, and Jairo Sinova, Phys. Rev. Lett. **105**, 227201 (2010).

[9] P. Nemec, V. Novak, N. Tesarova, E. Rozkotava, H. Reichlova, D. Butkovicova, F. Trojanek, K. Olejnik, P. Maly, R. P. Campion, B. L. Gallagher, Jairo Sinova, and T. Jungwirth, Nat. Commun. **4**, 1422 (2013).

[10] T. Jungwirth, J. Sinova, A. H. MacDonald, B. L. Gallagher, V. Novák, K. W. Edmonds, A. W. Rushforth, R. P. Campion, C. T. Foxon, L. Eaves, E. Olejník, J. Mašek, S.-R. Eric Yang, J. Wunderlich, C. Gould, L. W. Molenkamp, T. Dietl, and H. Ohno, Phys. Rev. B **76**, 125206 (2007).

[11] J. Mašek, F. Máca, J. Kudrnovský, O. Makarovsky, L. Eaves, R. P. Campion, K. W. Edmonds, A. W. Rushforth, C. T. Foxon, B. L. Gallagher, V. Novák, Jairo Sinova, and T. Jungwirth, Phys. Rev. Lett. **105**, 227202 (2010).

[12] C. Timm, J. Phys.: Condens. Matter **15**, R1865 (2003).

[13] F. Popescu, C. Sen, E. Dagotto, and A. Moreo, Phys. Rev. B **76**, 085206 (2007).

[14] M. Turek, J. Siewert, and J. Fabian, Phys. Rev. B **78**, 085211 (2008).

[15] G. Alvarez and E. Dagotto, Phys. Rev. B **68**, 045202 (2003).

[16] C. P. Moca, G. Zarand, and M. Berciu, Phys. Rev. B **80**, 165202 (2009).

[17] S.-R. Eric Yang, J. Sinova, T. Jungwirth, Y. P. Shim, and A. H. MacDonald, Phys. Rev. B **67**, 045205 (2003).

[18] W. W. Chow and S. W. Koch, *Semiconductor-Laser Fundamentals: Physics of the Gain Materials* (Springer-Verlag, Berlin, 1999).

[19] A. Richardella, P. Roushan, S. Mack, B. Zhou, D. A. Huse, D. D. Awschalom, and A. Yazdani, Science **327**, 665 (2010).

[20] J. M. Luttinger and W. Kohn, Phys. Rev. **97**, 869 (1955).

[21] D. J. Singh and D. A. Papaconstantopoulos, *Electronic Structure and Magnetism of Complex Materials* (Springer-Verlag, Berlin, 2002).

[22] A. K. Bhattacharjee and C. Benoit a la Guillaume, Solid State Commun. **113**, 17 (2000).

[23] A. X. Gray, J. Minar, S. Ueda, P. R. Stone, Y. Yamashita, J. Fujii, J. Braun, L. Plucinski, C. M. Schneider, G. Panaccione, H. Ebert, O. D. Dubon, K. Kobayashi, and C. S. Fadley, Nat. Mater. **11**, 957 (2012).

[24] I. Di Marco, P. Thunstrom, M. I. Katsnelson, J. Sadowski, K. Karlsson, S. Lebegue, J. Kanski, and O. Eriksson, Nat. Commun. **4**, 2645 (2013).

[25] M. Abolfath, T. Jungwirth, J. Brum, and A. H. MacDonald, Phys. Rev. B **63**, 054418 (2001).

[26] D. Kitchen, A. Richardella, J.-M. Tang, M. E. Flatte, and A. Yazdani, Nature (London) **442**, 436 (2006).

[27] J. Sinova, T. Jungwirth, J. Kucera, and A. H. MacDonald, Phys. Rev. B **67**, 235203 (2003).

[28] S.-R. Eric Yang and A. H. MacDonald, Phys. Rev. B **67**, 155202 (2003).

[29] J. T. Edwards and D. J. Thouless, J. Phys. C: Solid State Phys. **5**, 807 (1972).